Article

The Effect of Two Parallel Crack Inclination Angles on the Stability of Concrete Members under Dynamic Loading

Ahmad Moradpour [1], Mojtaba Hosseini [2]*, Hamidreza Babaali [3]

[1] PhD Candidate, Department of Civil Engineering, Khorramabad Branch, Islamic Azad University, Khorramabad, Iran.
[2] Associate Professor, Department of Civil Engineering, Lorestan University, Khorramabad, Iran.
[3] Assistant Professor, Department of Civil Engineering, Khorramabad Branch, Islamic Azad University, Khorramabad, Iran.

Abstract: Dynamic Realistic Failure Process Analysis (DRFPA) is a numerical software based on FEM it is firstly validated by comparing with the experimental test. Such validation is carried out under two consistent concrete specimens under uniaxial compression. After validation, DRFPA is used to study the influence of two parallel pre-existing crack inclination angles on the fracture of concrete under dynamic loads. The evolution of wing cracks and secondary cracks is investigated by observing the initiation, coalescence, and propagation of them. Meanwhile, the relationship between failure mode and inclination angles is discussed via analyzing the acoustic emission events. Finally, it is concluded the relationship between inclination angles of pre-cracks and performance/stability of concrete structure.

Keywords: Dynamic loadings; Inclination angles; Numerical simulation; Pre-cracked concrete

1. INTRODUCTION

Pre-cracked structure has studied considerably in both experimental and numerical fields in last few decades. Such studies covered rock structure [1], [2], masonry structure [3] and concrete structure [4]. In particular, two parallel pre-existing cracks in multiple materials have been studied to predict the performance/stability of those structures/materials by investigating the failure mode (tension failure/shear failure) and the evolution of cracks, such as the initiation, coalescence and propagation of wing cracks/secondary cracks [5-8].

In addition, many variables influencing the behavior of the pre-cracked concrete including the mechanical parameters [9] as well as rough surface properties [10] of it, inclination angles geometry [4] and loading methods [11], were investigated considerably. However, few studies covered three-phase (matrix, bond and aggregate) concrete with variable two parallel pre-existing cracks subjected to dynamic impact compressive stress wave [8].

In terms of model scale, many levels were involved in past studies, such as micro, meso and macroscopic level [12]. In general, an experimental model is used to assess concrete failures and investigate the evolution of cracks at a meso or macroscopic level. However, it is difficult to observe the internal crack evolution and failure mode under such study methodology [13]. Therefore, many numerical methodologies have been developed significantly to do advanced studies on pre-cracked reinforced/unreinforced concrete [14, 15]. Hsu proposed a theory related to softened truss model to realize numerical study [16]. Furthermore, Bazant and Ozbolt proposed another numerical method called nonlocal micro-plane model [17]. After that, they evolved their model via updating the function of adding single pre-crack [18]. However, it is difficult to simulate the heterogeneous and

 doi:10.20944/preprints202211.0310.v2

some mechanical parameters of material via many common numerical models, and above-mentioned models could not setup multiple pre-cracks, and they were not adopted to apply dynamic loadings. Tang developed a new numerical software to make up those mentioned disadvantages based on the finite element called RFPA [19], and there was also a dynamic version (DRFPA).

After this introduction, the following Section 2 is related to basic constitutive relationship of DRFPA. Section 3 detailed describes the numerical model setup. In Section 04, the numerically simulated results are analyzed in detail. Section 05 presents the conclusions.

2. Description of DRFPA

Realistic Failure Process Analysis (RFPA) was proposed by Tang [18] and had been evolved considerably. Based on it, a dynamic version was developed, abbreviated as DRFPA. Such software was established on finite element theory and statistic damage theory to numerically simulate progressive fracture and instability of quasi-brittle rock-like materials under either dynamic or static loadings at the mesoscopic level [8]. Compared with other numerical software or experimental specimens, the advantage of current software is that the inhomogeneity of material properties can be digitized to simulate the nonlinearity of material itself [8]. Meanwhile, the mechanical problems of discontinuous media can be solved based on a continuum mechanics method. The mechanical properties (e.g., elastic modulus, strength and Poisson's ratio) of three-phase (matrix, bond and aggregate) concrete specimens are assumed to follow the Weibull distribution which can be defined as probability density function proposed by Weibull [8], [20-21]:

$$f(u) = \frac{m}{u_0}\left(\frac{u}{u_0}\right)^{m-1} \exp\left[-\left(\frac{u}{u_0}\right)^{m}\right] \tag{1}$$

Where, u is a given mechanical property, u_0 is the parameters of scale, m is a parameter related to the shape of distribution function. It should be noted that m is related to homogeneity index, that is, the material becomes more homogeneous when it is assigned a larger value [8].

2.1. Constitutive Relationship of DRFPA

First of all, the elastic damage mechanics must be considered according to constitutive relationship of the elements for both tensile and shear damage conditions. The elastic modulus of damaged material can be expressed as follows [8, 12]:

$$E = (1 - D)E_0 \tag{2}$$

Where, E and E_0 denote damaged and undamaged materials related to elastic modulus, respectively [8]. D is damage which can be divided into D_+ (tensile damage) and D_- (shear damage). It should be noted that above three terms are all scalars since it is assumed the damage of element is isotropic elasticity. In addition, at the beginning of simulation, D=0, that is because there is no initial damage being contained, simultaneously, the stress-strain curve is linear elastic without damage occurring in such model [8].

According to Zhu et al. [12], in terms of uniaxial tension, considering the damage evolution of element [22], the constitutive relationship under static loading condition at the mesoscopic level can be expressed as below [23]:

$$D = \begin{cases} 0 & \varepsilon < \varepsilon_{t0} \\ 1 - \dfrac{\lambda\varepsilon_{t0}}{\varepsilon} & \varepsilon_{t0} < \varepsilon < \varepsilon_{tu} \\ 1 & \varepsilon \geq \varepsilon_{tu} \end{cases} \tag{3}$$

Where, λ is the coefficient of residual strength which can be defined by $f_{tr} = \lambda f_{t0}$, f_{tr} is residual tensile strength, f_{t0} and is uniaxial tensile strength. ε_{t0} Is threshold strain which

Preprints (www.preprints.org) | NOT PEER-REVIEWED | Posted: 21 November 2022 doi:10.20944/preprints202211.0310.v2

represents the elastic limit of strain [8, 24]? ε_{tu} Is ultimate tensile strain which is defined by$\varepsilon_{tu} = \eta\varepsilon_{t0}$, η is ultimate strain coefficient. Therefore, according to above relationship, the element will be damaged when tensile strain of it reaches the ultimate value [8].

However, the above-mentioned constitutive relationship of uniaxial tension is considered as one dimensional. Therefore, an equivalent three-dimensional method proposed by Mazars, and Pijaudier-Cabot was applied to expand the dimension from one to three [25]. Such function can be expressed as below [8, 26]:

$$\bar{\varepsilon} = \sqrt{\langle\varepsilon_1\rangle^2 + \langle\varepsilon_2\rangle^2 + \langle\varepsilon_3\rangle^2} \tag{4}$$

Where, ε_1, ε_2 and ε_3 are the main strains, respectively. $\bar{\varepsilon}$ is equivalent stain which is replaced by main strains. Equation (4) can be applied if and only if when the element satisfies the maximum tensile strain criterion to produce tensile damage. In addition, < > function can be defined as follows [8, 27]:

$$\langle x\rangle = \begin{cases} x & x \geq 0 \\ 0 & x < 0 \end{cases} \tag{5}$$

Thus, now (3) can be rewritten as [28]:

$$D = \begin{cases} 0 & \bar{\varepsilon} < \varepsilon_{t0} \\ 1 - \dfrac{\lambda\varepsilon_{t0}}{\varepsilon} & \varepsilon_{t0} < \bar{\varepsilon} < \varepsilon_{tu} \\ 1 & \bar{\varepsilon} \geq \varepsilon_{tu} \end{cases} \tag{6}$$

Nevertheless, above constitutive relationship only covers elastic damage aspect at the mesoscopic level. In fact, damage of element also exists when it is under uniaxial compression or shear stress [29]. In current paper, it is assumed the shear damage is also at the mesoscopic level under such stress [30]. Thus, Mohr-Coulomb criterion can be used to be the second damage threshold [31-32]:

$$F = \frac{1 + \sin\phi}{1 - \sin\phi}\sigma_1 - \sigma_3 \geq f_{c0} \tag{7}$$

Where, ϕ is internal friction angle of element, f_{c0} is uniaxial compressive strength of that as a positive number. σ_1 and σ_3 are maximum and minimum principal stress, respectively. Above parameters are all at the mesoscopic level [8].

In this way, the constitutive relationship of uniaxial compressive stress is easy to derive [12]:

$$D = \begin{cases} 0 & \varepsilon > \varepsilon_{c0} \\ 1 - \dfrac{\lambda\varepsilon_{c0}}{\varepsilon} & \varepsilon \leq \varepsilon_{c0} \end{cases} \tag{8}$$

Here, λ is the residual strength coefficient of elements and it is satisfied the following relationship: $= \frac{f_{cr}}{f_{c0}} = f_{tr}/f_{t0}$. ε_{c0} Is maximum compressive principal strain. ε_{c0} Is maximum compressive principal strain and it can be described as below [33]:

$$\boldsymbol{\varepsilon_{c0}} = \frac{-\mathbf{f_c}}{\mathbf{E_0}}. \tag{9}$$

Meanwhile, when element is under multi-axial stress state, it satisfies the Mohr-Coulomb criterion as well. The maximum compressive principal strain ε_{c0} can be expressed as follows [34]:

$$\varepsilon_{c0} = \frac{1}{E_0}\left[-f_{c0} + \frac{1 + \sin\phi}{1 - \sin\phi}\sigma_1 - \mu(\sigma_1 + \sigma_2)\right] \tag{10}$$

Where, μ is Poisson's ratio [8].

 doi:10.20944/preprints202211.0310.v2

Meanwhile, the maximum compressive principal strain ε_3 can be substituted into (8) when element is under multi-axial stress state and satisfies the Mohr-Coulomb criterion at the same time [35]. Now, one dimensional relationship can be extended to three-dimensional. The damage variable D is expressed as below [8]:

$$D = \begin{cases} 0 & \varepsilon_3 > \varepsilon_{c0} \\ 1 - \dfrac{\lambda \varepsilon_{c0}}{\varepsilon_3} & \varepsilon_3 \le \varepsilon_{c0} \end{cases} \tag{11}$$

In addition, the constitutive relationship of element is expressed based on the elastic mechanics. There is no damage occurring when element is unloaded or reloaded. Thus, elastic modulus of materials will be constant, and element will keep residual deformation when all elements are unloaded, or in other word, all stresses are released. In current paper, the element is constantly damaged, and material properties of element are continuously weakened although there is only one constitutive relationship considering. Meanwhile, a repeated calculation will be processed under a constant external loading condition when an element fails in a loading step until there is no element damaging. It can be seen as an iterative process, called step-in-step function [8].

2.2. Strain-Rate Damage

Mohr-Coulomb criterion can be applied under dynamic loading condition when increment of cohesion of with strain rate is counted [8, 36]. A semi-log function is expressed as follows to describe the relationship between dynamic uniaxial compressive strength and loading rate [37]:

$$f_{cd} = A \log\left(\dot{f}_{cd}/\dot{f}_{c0}\right) + f_{c0} \tag{12}$$

Where, f_{cd} is dynamic uniaxial compressive strength in MPa, $\dot{f}_{cd}$ is dynamic loading rate in MPa/s. $\dot{f}_{c0}$ Is quasi-brittle loading rate and it is approximately equal to 5×10^{-2} MPa/s, f_{c0} is uniaxial compressive strength at quasi-static loading rate. A is strain rate parameter which effects dynamic strength. The value of it in terms of different materials are detailed discussed in previous paper [8, 38].

2.3. Finite Element Implementation

Zhu and Tang indicated that the equilibrium equation governed the linear dynamic response of the finite element system which can be expressed as below [8, 39]:

$$M\ddot{U} + C\dot{U} + KU = R(t) \tag{13}$$

Where, M, C and K are mass, damping and stiffness, respectively. R(t) is vector of externally applied loadings or unbalanced force. U, $\dot{U}$ and $\ddot{U}$ are nodal displacement, velocity and acceleration, respectively. In terms of some other assumptions, such as Rayleigh damping and Wilson θ method of implicit time integration, detailed discussion and description are covered in previous paper [8, 38].

In addition, for dynamic response problem, the maximum time step is related to the wave speed in material and size of the finite element. In this way, the maximum time step can be selected, and then the stress wave cannot propagate beyond the distance between integration points of elements in time increments [8].

2.4.(. AE) Principal

The principal of acoustic emission (AE) is necessary to clarify [8]. Such function is used to monitor the crack/fracture processes forming in some portions of concrete specimens [40]. In current software, it is assumed that the (AE) events will occur when element fails because the elastic energy stored in element must be released during the deformation

 doi:10.20944/preprints202211.0310.v2

happening [8]. Therefore, DRFPA is able to simulate (AE) activities, such as rate, magnitude and location of (AE) events, by recording the released energy and damaged count of elements. The accumulative damage D can be calculated as follows [8, 41]:

$$D = \frac{1}{N}\sum_{i=1}^{s} n_i \tag{14}$$

Where "s" is the number of calculated steps, "n_i" is the damaged elements in the nth step, "N" is the total elements of simulated model [8].

Additionally, the release of energy can be calculated as follows when element fails [8, 42]:

$$W_i = \frac{1}{2E}(\sigma_1^2 + \sigma_3^2 - 2\nu\sigma_1\sigma_3)V \tag{15}$$

Where, "i" is number of elements, "W_i" is released elastic strain energy, "E" is elastic modulus, σ_1 and σ_3 are maximum and minimum principal stress, respectively. "ν" Is Poisson ratio; "V" is the element volume [8, 42].

2.5. Static Verification of Numerical Model

The DRFPA is verified by comparing the numerically simulated results with the corresponding experimental results under static loadings [8]. The dimension of concrete specimen is 100mm long and 100mm high. The mechanical parameters related to elastic modulus, uniaxial compressive strength and homogeneity index of experimental three-phase concrete are shown in Table I. Failure patterns of both experimental and numerical results are illustrated in Fig 1. It should be noted that the specimen is simulated under uniaxial compression [43].

TABLE I. Mechanical Parameters of Experimental Three-Phase Concrete [8, 44].

Phase	Elastic modulus (GPa)	Uniaxial compressive strength (MPa)	Homogeneity index m
Matrix	28.6	175	3
Bond	15	150	1.5
Aggregate	80	500	6

A B

Fig 1 Failure patterns of concrete specimen under uniaxial compression: (a) experimental result; (b) numerical result [8, 44].

According to Fig 1, the failure mode of numerical simulation is in agreement with that of experimental result. However, it should be noted that the evolution of cracks is not idealized consistent. This is because the heterogeneity of concrete three-phase is difficult to determine in terms of experimental model.

3. Numerical Model Setup

Preprints (www.preprints.org) | NOT PEER-REVIEWED | Posted: 21 November 2022 doi:10.20944/preprints202211.0310.v2

The pre-cracked concrete specimens with 200mm high, 100mm wide and 1mm thick are numerically formed two parallel pre-existing cracks before simulation. Such cracks are 30mm long and 1mm thick which are located at the center of the specimen and the internal tips of them are 40mm apart in the vertical direction as show in Fig 2(a) [45]. Where, α is the inclination angle measured from horizontal plane to pre-cracks while β is that of the concrete bridge. Table II shows α and β variables related to specimens. It should be noted that ligament length (i.e., the distance between two internal flaw tips) will vary according to the change of β [46]. Concrete specimens are three-phase, including matrix, bond and aggregate. Related mechanical parameters of them are referred to Table III [12].

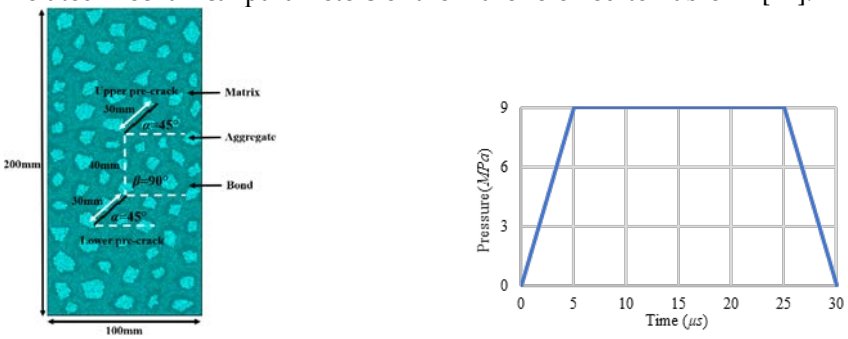

A B

Fig 2 (a) Specimen model; (b) Applied dynamic impact compressive stress wave [8, 38].

In addition, some basic assumptions and numerical simulation parameters are necessary to be clarified. First of all, all involved mechanical parameters of three-phase are followed Weibull distribution. Meanwhile, the element constitutive parameters are covered such as softening scheme of the constitutive curve, residual strength coefficient and friction angle. Secondly, as mentioned in Section 02, the relationship of element related to both compressive strength and tensile stress are considered to be close. Therefore, they all follow the same distribution in current paper, and the value of the tensile strength can be calculated automatically by software from multiplying the compressive strength value by the coefficient of tensile strength. Thirdly, in order to avoid the adverse effect of some important parameters on the results, it is set the same homogeneity of material related to elastic modulus and uniaxial compressive strength, following Weibull distribution as well [8].

Table II. α and β variables.

Specimen	α (°)	β (°)
I (reference term)	45	90
II	0	90
III	30	90
IV	60	90
V	90	90
VI	45	45
VII	45	60
VIII	45	120
IX	45	135

Furthermore, tensile strength ratio is 10, internal friction angle is constant at 30°. It should be noted that the dispersion of Poisson's ratio is relatively small, thus, its homogeneity and average value are 100 and 0.2, respectively. Finally, according to previous paper of Wang et al. [38], a dynamic impact compressive stress wave is applied to the specimens to implement dynamic simulation. The frequency of wave and magnitude of pressure related to such wave are illustrated in Fig 2(b). All specimens will be numerically simulated

Preprints (www.preprints.org) | NOT PEER-REVIEWED | Posted: 21 November 2022 doi:10.20944/preprints202211.0310.v2

1500 steps (150 microseconds) and step-in-step function will be used to identify the difference between tension failure and shear failure [8].

Table I. Mechanical Parameters Of Three-Phase Concrete Specimens [8, 12]

Phase	Elastic modulus (GPa)	Uniaxial compressive strength (MPa)	Homogeneity index m
Matrix	27.30	165	3.0
Bond	11.44	70	3.0
Aggregate	80.00	500	6.0

4. Numerical Results And Analysis

To understand the influence of inclination angles related to pre-cracks on fracture of concrete, nine series of specimens are numerically simulated through DRFPA to investigate the initiation, coalescence and propagation of wing cracks as well as secondary cracks, meanwhile, AE energy and counts captured by DRFPA are also discussed [8].

4.1. Reference Term (α=45°, β=90°)

When α=45°, β=90°, through the AE distribution patterns as shown in Fig 3 [32] (AE), it is easy to find that AE events firstly occur near the bond phase when dynamic impact compressive stress wave passes through the specimen. In particular, massive energy release (AE events) is captured concentrating the tips of pre-cracks, especially for upper pre-crack. Correspondingly, shear stress is also concentrated near those areas, thus, crack forms as shown in Fig 3 (Stress, Cracks) [8].

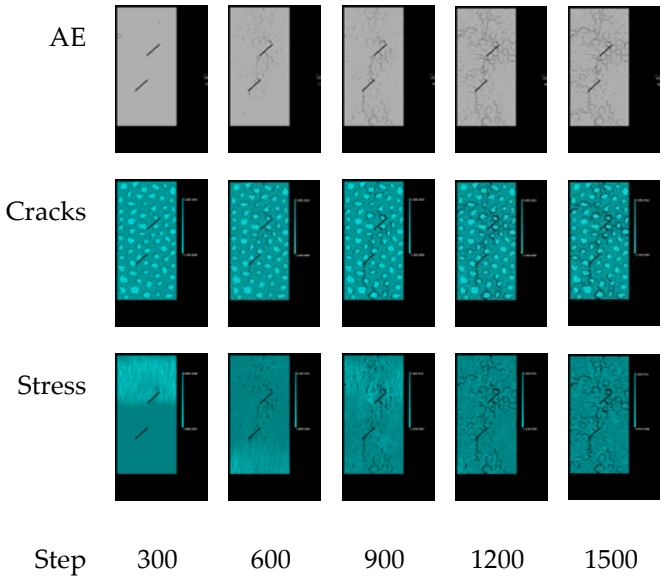

Fig 3 The distribution patterns of AE, cracks and shear stress when α=45°, β=90°.

According to the crack distribution patterns, it is found that, under current inclination angles geometric condition, micro cracks obviously initiate from nearby tips of pre-cracks, then, along with subjecting to the continuous dynamic wave and its reflected wave

 doi:10.20944/preprints202211.0310.v2

[8], such cracks coalesce into larger scale cracks called wing cracks. After that, wing cracks propagate along the direction parallel to the applied dynamic loadings [47].

In addition, in terms of secondary cracks, it is found some oblique second cracks are forming below the upper pre-crack at the same time as the wing cracks forming. However, in contrast, there is no obvious quasi-coplanar secondary crack initiating nearby neither upper pre-crack nor lower pre-crack. This may be related to the angle between α/β and the direction of dynamic loadings, which needs to be proved in Section 4.2 and 4.3 [48].

4.2. α. Variables

In order to clarify the influence of α on initiation, coalescence and propagation of wing cracks and secondary cracks, four series specimens are numerically simulated by investigating α variables.

4.2.1.α=0°

When α=0°, compared with reference term, Fig 4 shows that wing cracks are not obviously initiate. There are only few cracks initiating and propagating along the bond phase on the outside of two pre-cracks, that is above the upper pre-crack and below the lower pre-crack. Meanwhile, for concrete bridge area, there are some micro cracks initiating near the internal tips of pre-cracks, while such cracks tardily and steadily coalesce and propagate along the bond phase, forming small scale wing cracks. After 1500 steps simulation, those wing cracks initiated from upper and lower internal tips do not intersect [8, 47].

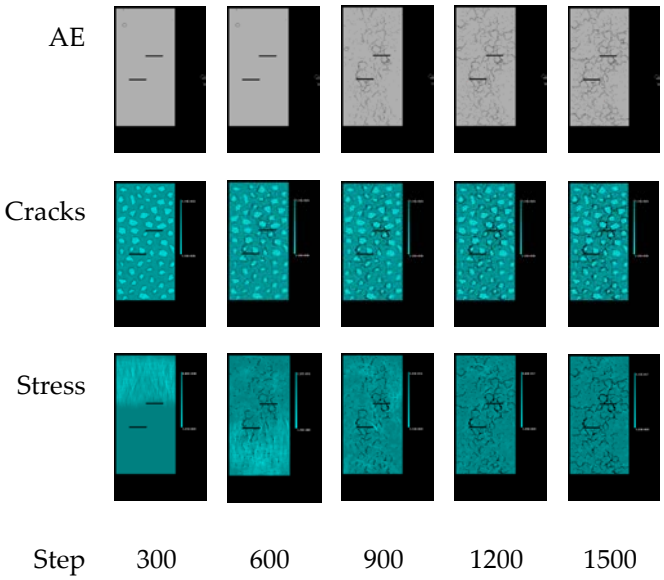

Fig 4 The distribution patterns of AE, cracks and shear stress when α=0°, β=90°.

In addition, it is obviously found that oblique second cracks initiate from the external tip of lower pre-crack, and such cracks propagate parallel to the direction of dynamic loadings [8, 49]. It should be noted that such cracks coalesce tardily at the earlier stage of dynamic loadings, while it propagates significantly when reflected wave reaches the lower pre-crack. Meanwhile, micro cracks only slightly initiate at the external tip of upper pre-crack, forming very slight quasi-coplanar secondary cracks with continuous dynamic loadings and its reflected wave.

4.2.2. α=30°

When α=30°, as shown in Fig 5, the wing cracks of concrete bridge are significantly initiate and propagate over time, causing obvious fracture within such zone. In the meantime, some micro cracks initiated from external tips of both upper and lower pre-cracks

 doi:10.20944/preprints202211.0310.v2

coalesce tardily and steadily before 60μs (Step: 600). Those micro cracks propagate along the bond phase, forming minor wing cracks and quasi-coplanar secondary cracks near the external tip of upper pre-crack (90μs, Step: 900). Similarly, there are also minor quasi-coplanar secondary cracks initiating and propagating from the external tip of lower pre-crack. However, there is no wing crack initiating from such position [8, 50].

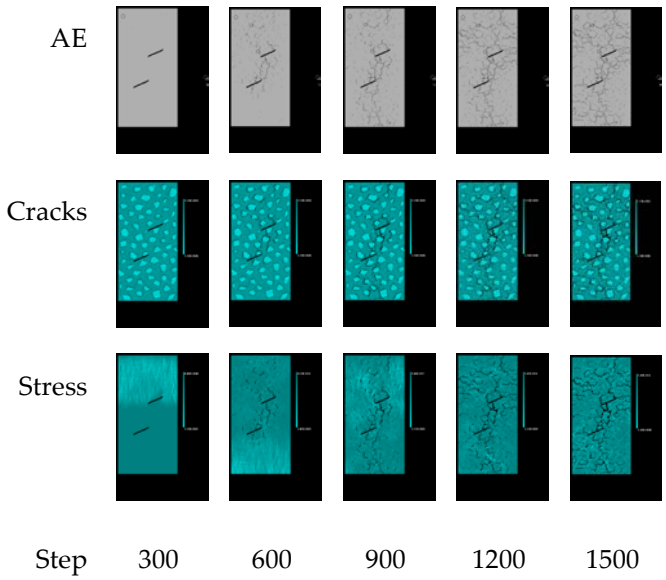

Fig 5 The distribution patterns of AE, cracks and shear stress when α=30°, β=90°.

In terms of oblique second cracks, such cracks initiated from the internal tips of both upper and lower pre-cracks dramatically coalesce and propagate along the direction parallel to the applied dynamic loadings [8]. Their propagation spread to the top face and bottom face of concrete specimen, showing a radial crack distribution pattern, when specimen is subjected to dynamic wave and its multiple reflected waves, respectively [51].

4.2.3. α=60°

When α=60°, Fig 6 illustrates the AE events, crack distribution patterns and shear stress distribution, respectively.

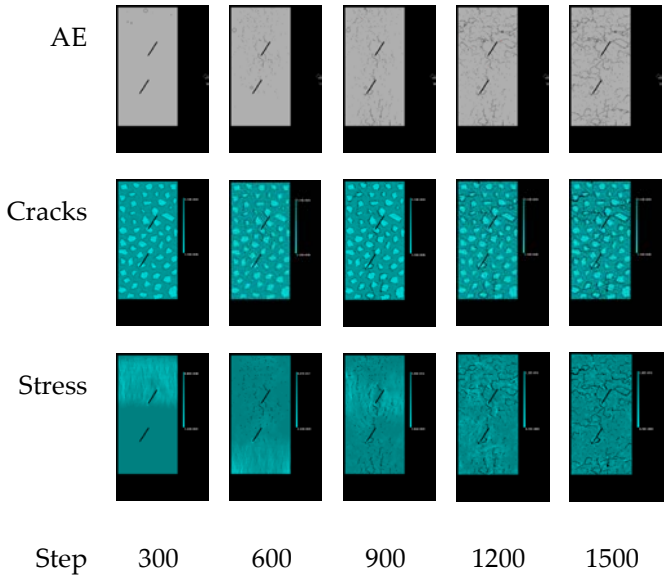

Fig 6 The distribution patterns of AE, cracks and shear stress when α=60°, β=90°.

 doi:10.20944/preprints202211.0310.v2

From the Fig 6 (AE), it is obvious that the AE events are concentrated in upper part of the specimen. There are only minor AE events being captured near the bottom face of concrete specimen caused by the reflected wave. Therefore, it is found some micro cracks initiate near the tips of upper pre-cracks when t=90μs (Step: 900). Such micro cracks coalesce and transform into wing cracks and oblique second cracks over time. They all propagate along the bond phase whose direction is perpendicular to the applied dynamic loadings. In addition, the wing cracks of concrete bridge are mildly initiate and propagate over time, causing minor fracture within such zone. In the meantime, in terms of the evolution of cracks near lower pre-crack, there are only some minor micro cracks initiating from tips of it, not coalescing into large-scale cracks, regardless of wing cracks or secondary cracks [8].

4.2.4. α=90°

When α=90°, as shown in Fig 7, it is similar with the case when α=60°. According to the Fig 7 (AE), more AE events are concentrated in upper part of the concrete specimen than that of lower part. Compared the evolution of cracks from upper pre-crack with that of lower pre-crack, the micro cracks initiated from external tip of upper pre-crack transform into wing cracks and then propagate along the direction perpendicular to the applied dynamic loadings. However, the wing cracks formed from external tip of lower pre-crack propagate along the direction parallel to the applied dynamic loadings. In terms of the wing cracks within concrete bridge, some micro cracks initiate near the internal tips of both upper and lower pre-cracks, whereas such micro cracks do not coalesce into wing cracks before 150μs (Step: 1500). Meanwhile, it is found significant oblique second cracks initiate and propagate from external tip of upper pre-crack. The direction of it is opposite to that of wing cracks. In addition, it is not found significant quasi-coplanar secondary cracks forming from neither upper nor lower pre-cracks within 150μs simulation [8, 52-53].

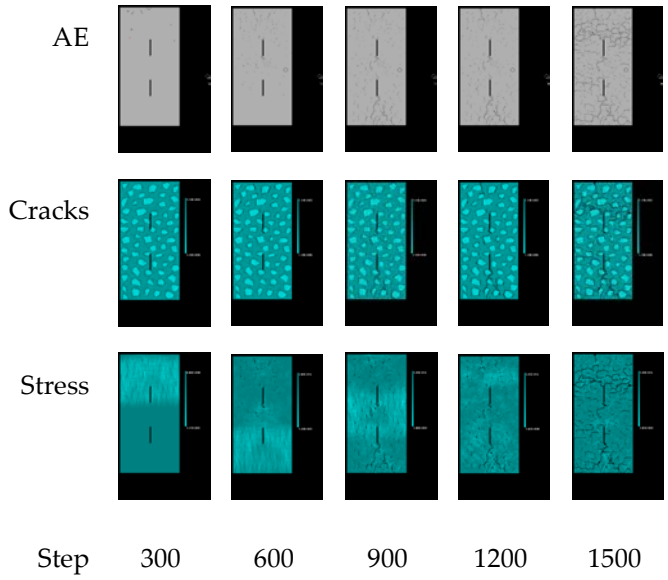

Fig 7 The distribution patterns of AE, cracks and shear stress when α=90°, β=90°.

4.3. β. Variables

Similarly, in order to clarify the influence of β on initiation, coalescence and propagation of wing cracks and secondary cracks, four series specimens are numerically simulated by investigating β variables [54].

Preprints (www.preprints.org) | NOT PEER-REVIEWED | Posted: 21 November 2022 doi:10.20944/preprints202211.0310.v2

4.3.1. β=45°

When β=45°, as shown in Fig 8, according to Fig 8 (AE), AE events are originally concentrated in tips of pre-cracks, forming micro cracks when t=60μs (Step: 600). After that, concrete specimen is subjected to reflected wave, and more AE events occur at the upper part of it (t=90-150μs, Step: 900-1500). From the Fig 8 (Cracks) (Shear), it is found that those micro cracks initiated from tips of pre-cracks coalesce and transform into wing cracks over time. In particular, it is also observed that oblique second cracks form from the internal tip of upper pre-crack, and they propagate along the direction parallel to the applied dynamic loadings. In the meantime, there are significant quasi-coplanar secondary cracks initiating and coalescing from both internal tips of pre-cracks within the concrete bridge. The propagation of such cracks is along the bond phase [8, 50].

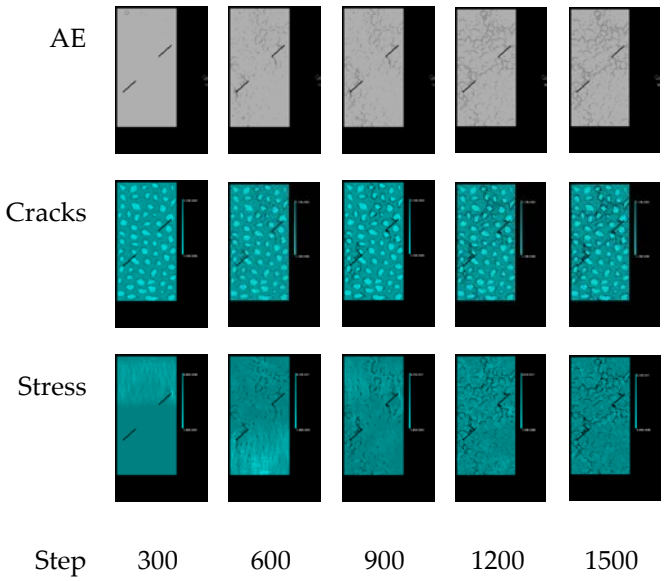

Fig 8 The distribution patterns of AE, cracks and shear stress when α=45°, β=45°.

In addition, in terms of those cracks propagating in the upper part of specimen, it is considered to cause partial damage/fracture of concrete. This is because the ligament length is too long to effectively block the propagation of reflected wave/secondary reflected wave inside the specimen.

4.3.2. β=60°

When β=60°, Fig 9 (AE) shows the AE events distribution patterns. Compared with previous case (β=45°), the distribution of AE events is more even. This is because as the β increases, the ligament length of concrete bridge gradually decreases, which effectively prevents the reflected wave from propagating in concrete specimen.

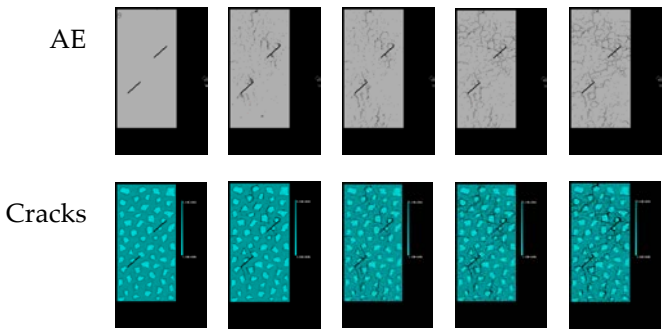

Preprints (www.preprints.org) | NOT PEER-REVIEWED | Posted: 21 November 2022 doi:10.20944/preprints202211.0310.v2

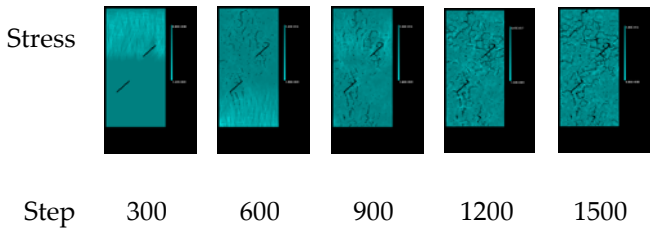

Fig 9 The distribution patterns of AE, cracks and shear stress when α=45°, β=60°.

The wing cracks initiate from external tips of both upper and lower pre-cracks significantly. However, in terms of the wing cracks initiated from internal tips of pre-cracks, it is relative minor. In the meantime, for external tips of pre-cracks, there are some micro cracks initiating there as shown in Fig 9 (Cracks) when t=120μs (Step: 1200). Such micro cracks tardily and steadily coalesce and transform into oblique second cracks, shown in Fig 9 (Cracks) when t=150μs (Step: 1500). In addition, there is no quasi-coplanar secondary cracks forming near neither internal nor external tips of pre-cracks [8].

4.3.3. β=120°

When β=120°, as shown in Fig 10, according to the AE distribution of Fig 10, it is found that the AE events are mainly concentrated on the central axis of the specimen at the first 90μs (first 900 steps) [32]. When t=1200μs (Step: 1200), AE events are significantly distributed through the entire specimen except for concrete bridge, and there are little changes of such events since then (t=1500μs, Step: 1500). It is observed significant wing cracks initiating and coalescing from the external tips of pre-cracks. In terms of concrete bridge, there are some minor cracks propagating along the bond phase. Such cracks do not form any wing cracks or secondary cracks. In addition, it is not found secondary cracks during the 150μs (Step: 1500) progress [8, 55].

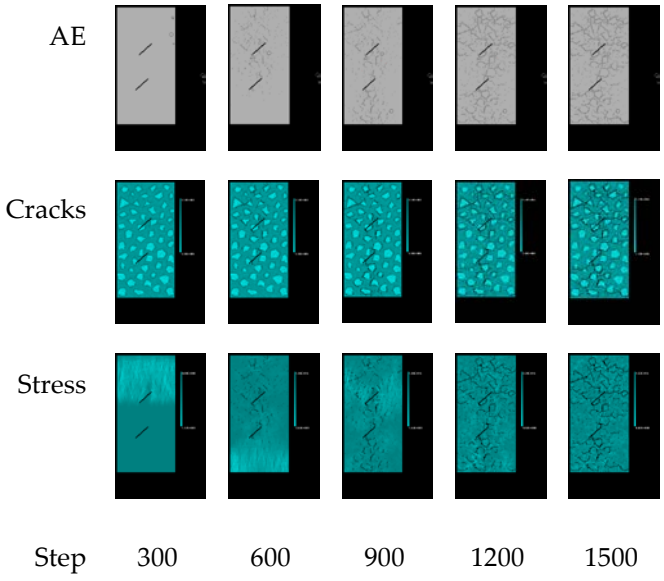

Fig 10 The distribution patterns of AE, cracks and shear stress when α=45°, β=120°.

4.3.4. β=135°

When β=135°, Fig 11 (AE) shows the AE events distribution patterns. Compared with previous case (β=120°), the distribution of AE events is concentrated in concrete bridge at first 60μs (Step: 0-600).

 doi:10.20944/preprints202211.0310.v2

Correspondingly, the wing cracks of concrete bridge initiate and coalesce in such zone. After that, the wing cracks form from the external tip of lower pre-crack as significant AE events occur (90μs, Step: 900) [56]. When t=1200-1500μs (Step: 1200-1500), wing cracks occur simultaneously in AE activities, initiating and coalescing from external tip of upper pre-crack. Similarly, with previous cases, the secondary cracks are not very obvious, only for the external tip of lower pre-crack, there are some oblique second cracks propagating along the bond phase.

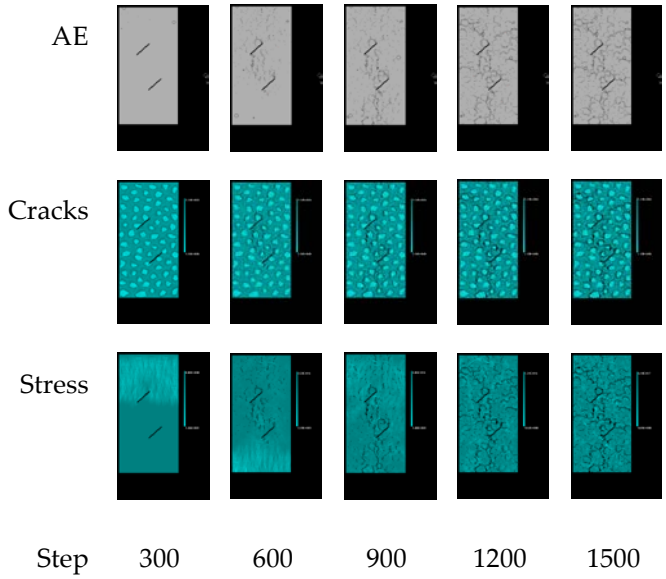

Fig 11 The distribution patterns of AE, cracks and shear stress when α=45°, β=135°.

4.4. AE Energy and Count

According to Table IV and Table *VI*, the events of AE energy and counts are always simultaneous, and their varies of magnitude are simultaneous as well. Meanwhile, the peaks of them are simultaneous. These phenomena are all consistent with the theory of current software. Therefore, it can be an effective way to investigate the process of crack initiation, coalescence and propagation, and the damage/fracture of specimens by analyzing the AE energy and counts.

4.4.1α. Variables

On the first hand, from Table IV, it is found the first peaks of AE energy and counts are postponed with increase of α. According to the shear stress distribution patterns as shown in from Fig 3 to Fig 7, the first peak is caused by dynamic impact compressive stress wave reaching the lower face of specimens and forming a reflected wave, such reflected wave damages the lower face of specimens, then lots of cracks initiate nearby there, and they propagate along the bond phase. Thus, it is easy to find that the magnitude of α can influence the dynamic impact compressive stress wave propagation speed. That is, the larger the α, the slower the speed of dynamic wave propagates. Generally, the second peaks of AE energy and counts are much higher than that of first peaks. This is because the reflected wave reaches the pre-cracked zone and forms the element failure with plenty energy release. During this progress, previous micro cracks caused by dynamic impact compressive stress wave transform into wing cracks or secondary cracks by taking secondary damage from reflected wave. The third peaks of AE energy and counts are caused by the secondary reflected wave. Such wave again passes through the pre-cracked zone that has been partially damaged. According to the value of the third peak, regardless of

Preprints (www.preprints.org) | NOT PEER-REVIEWED | Posted: 21 November 2022 doi:10.20944/preprints202211.0310.v2

the AE energy or the counts, it is found that AE events become more active as the α increases, that is, more energy is released, and the damage/fracture of specimens is more serious. On the other hand, according to

TABLE *V*, it is illustrated the relationship between α and AE energy, counts as well as their accumulative value. It is found that the peak value of AE energy and counts generally increases as α increases, while the total value of AE energy and counts decreases. That is, the damage/fracture of specimens is more serious with smaller α because the AE energy release directly represents the failure level of specimen. Furthermore, compared with the trend of peak value related to AE energy and counts as shown in Table IV, it is clear that the released energy and captured counts of AE increase with the number of reflected waves increasing, forming more serious damage/fracture of specimens. Therefore, it is predicted that in terms of pre-cracked concrete specimens subjected to dynamic impact compressive stress wave in a short time, the damage/fracture of specimens will be more severe with smaller α. Conversely, when specimens are under such dynamic loadings for a relative long time, the damage/fracture of them is milder as α decreases [8].

Table IV. AE energy as well as counts and their accumulative value. (α variable) [8].

α	AE energy and its accumulative value	AE count and its accumulative value
0°	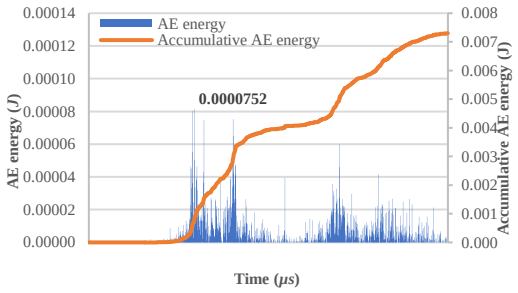	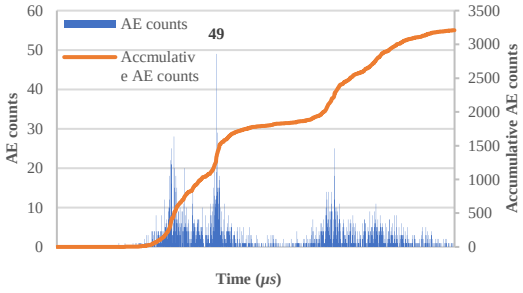
30°	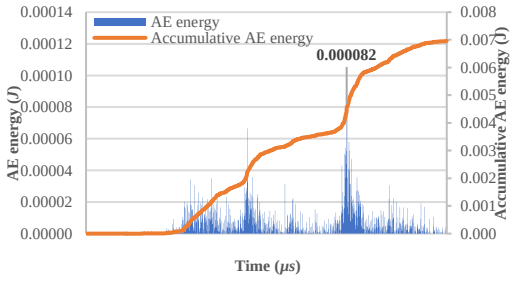	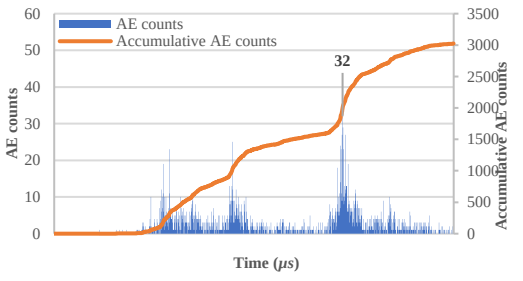
45°	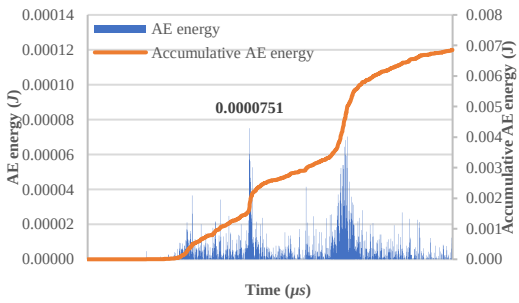	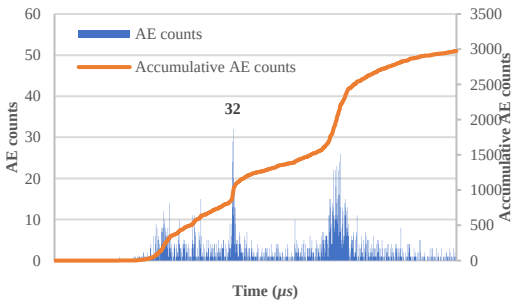

Preprints (www.preprints.org) | NOT PEER-REVIEWED | Posted: 21 November 2022 doi:10.20944/preprints202211.0310.v2

60°

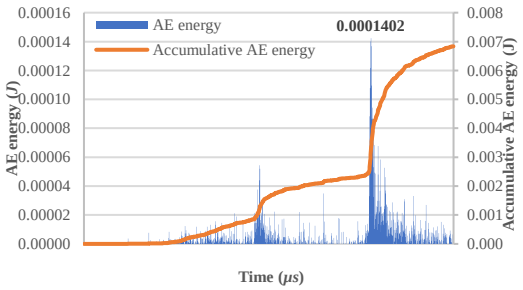

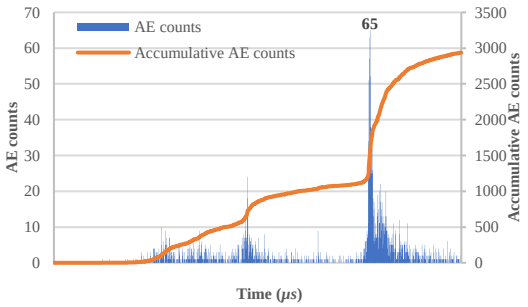

90°

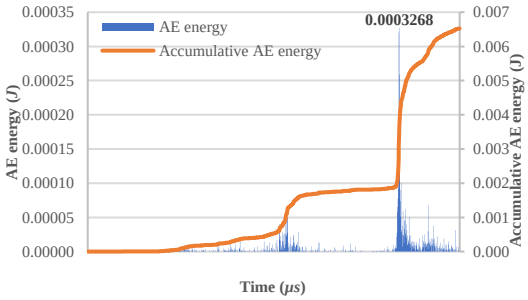

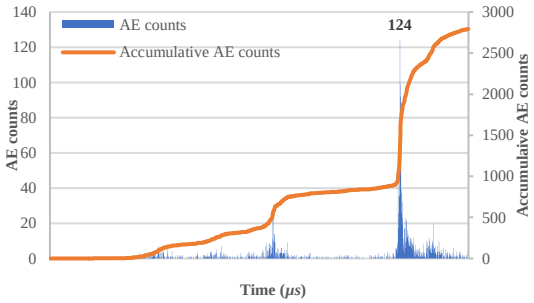

Table V. Peak AE energy as well as counts and their total value (α variable).

α	Peak AE energy (J)	Peak AE counts	Total AE energy (J)	Total AE counts
0°	0.0000813	49	0.0073016	3209
30°	0.0000820	32	0.0069579	3025
45°	0.0000751	32	0.0068546	2974
60°	0.0001402	65	0.0068341	2936
90°	0.0003268	124	0.0065246	2795

Table II. AE energy as well as counts and their accumulative value. (β variable) [8]

β	AE energy and its accumulative value	AE count and its accumulative value

Preprints (www.preprints.org) | NOT PEER-REVIEWED | Posted: 21 November 2022 doi:10.20944/preprints202211.0310.v2

45°

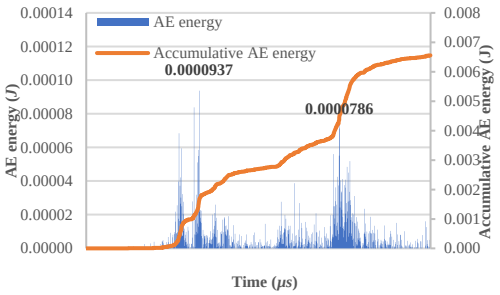

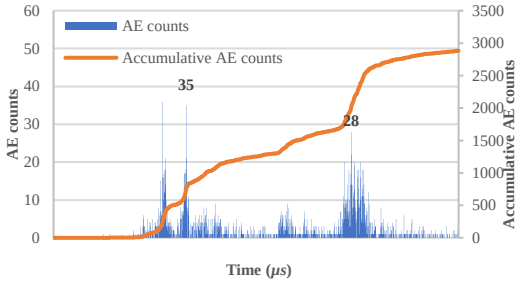

60°

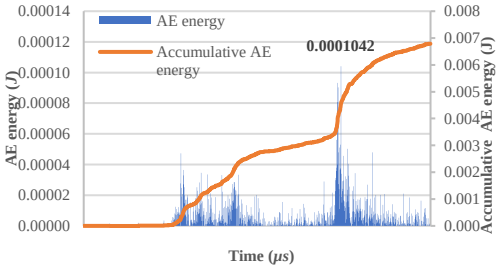

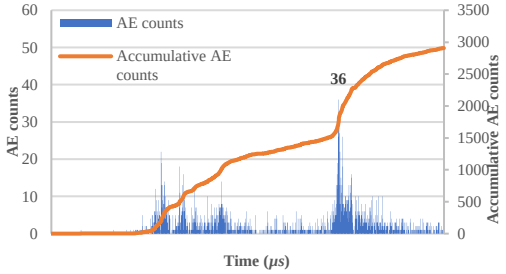

90°

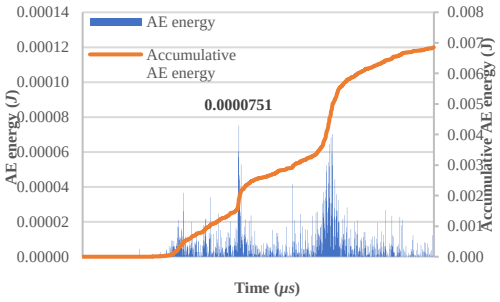

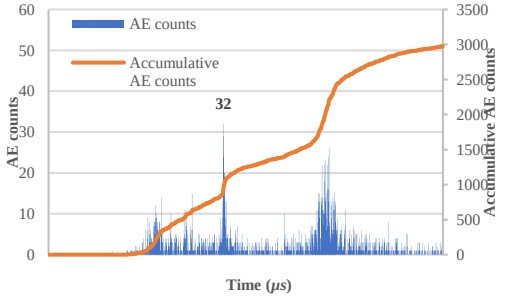

120°

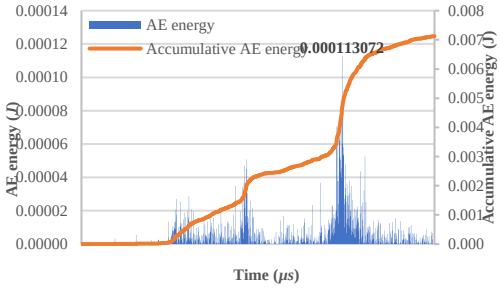

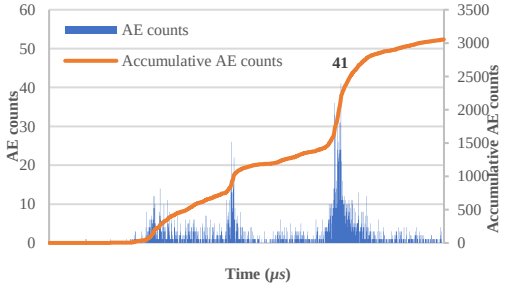

Preprints (www.preprints.org) | NOT PEER-REVIEWED | Posted: 21 November 2022 doi:10.20944/preprints202211.0310.v2

135°

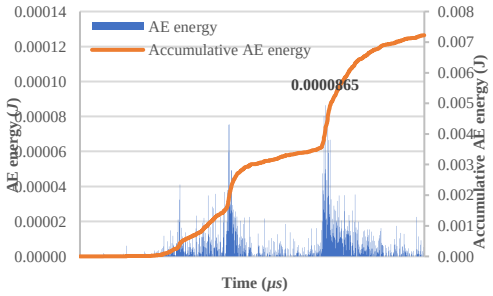

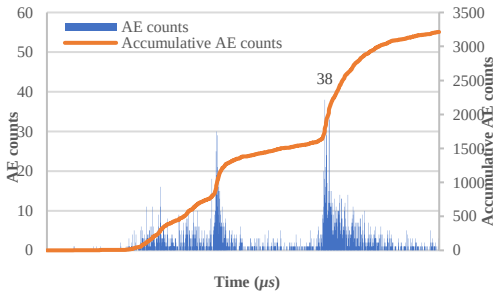

4.4.2. β. Variables

First of all, according to Table *VI*, compared with the influence of α on propagation speed of dynamic impact compressive stress wave, it is not found the first peaks of AE energy and counts are advanced or postponed with increment of β. According to the shear stress distribution patterns as shown in Fig 3 and from Fig 8 to Fig 11, it is similar with the explanation in Section 0, that is, the first peak is caused by the dynamic wave when it reaches the bottom of specimens and forms a reflected wave, then such wave causes energy release from each element nearby lower face of specimens, initiating lots of cracks and propagating along the bond phase. Therefore, it is concluded that the magnitude of β will not influence the dynamic impact compressive stress wave propagation speed.

In addition, in terms of β variables, the second peaks of AE energy and counts much differ from that of α variables. When β=45°, the second peaks of AE energy and counts do not form around 60 to 70μs when dynamic wave passes through the pre-cracked zone, as shown in

Table *VI* (45°). In other word, the reflected wave mildly damages the element nearby such zone, causing minor AE events. When β=60°, the second peaks of AE energy and counts are slightly lower than that of the first peaks. After that, the second peaks of AE energy and counts become higher than their own first peaks as β increases. In general, when β=90°, its second peaks value is the largest among all β variables. The reason for this phenomenon is because of the ligament length of concrete bridge. When ligament length increases, the reflected wave only causes mild damage in pre-cracked zone, forming minor AE events.

Finally, it is not found that the β variables have influence on AE events caused by secondary reflected wave. All AE counts value of the third peaks are approximately between 30 and 40, compared with the variety of data amplitude caused by the α variables, it is considered within the allowable data floating and drifting range. In summary, when the pre-cracked concrete specimens are subjected to dynamic impact compressive stress wave over time, the influence of β variables on the damage/facture of specimens is reduced. In the meantime, the influence on initiation, coalescence and propagation of cracks is reduced as well.

Table VII illustrates the peak value of AE energy and counts, and the total value of them. It is clearly indicated that the total AE energy and counts increase as β increases. In general, the pre-cracked concrete specimens will be more severely damaged under dynamic impact compressive stress wave with increment of β.

Table III . Peak AE energy as well as counts and their total value (β variable)

β	Peak AE energy (J)	Peak AE counts	Total AE energy (J)	Total AE counts

 doi:10.20944/preprints202211.0310.v2

45°	0.0000937	36	0.00655708	2883
60°	0.0001042	36	0.00678730	2907
90°	0.0000751	32	0.00685464	2974
120°	0.0001131	41	0.00712456	3054
135°	0.0000865	38	0.00722477	3213

5. Conclusion

Variable α and β related to two parallel pre-existing cracks of concrete are numerically simulated to investigate the relationship between such inclination angles and performance/stability of concrete structure via DRFPA. The evolution of wing cracks and secondary cracks, such as initiation, coalescence, and propagation of them are investigated. In the meantime, AE events are also analyzed to predict the performance/stability of concrete structure. Here are some conclusions as follows:

- The damage/fracture of concrete will be more minor as α increases. This is because the magnitude of α can influence the dynamic impact compressive stress wave propagation speed. That is, the larger α, the slower the speed of dynamic wave propagates.
- The damage/fracture of concrete will be more significant as β increases. This is because when the β is smaller, the ligament length of the concrete bridge is longer, thus the wing cracks in the bridge zone are difficult to coalesce and propagate. Furthermore, the change of β will not affect the propagation speed of the reflected waves.
- Compared with the secondary cracks, wing cracks are more significant. It is difficult to observe secondary cracks, especially for quasi-coplanar secondary cracks. The reason is the character of current software is that it only records tensile stress via step-in-step function, while shear stress will be recorded at the end of each single step. Theoretically, the secondary cracks can only be observed at such mentioned particular steps. At such steps, a few concentrated elements are damaged and release energy, forming secondary cracks at a macroscopic level. However, elements will be damaged in a large-scale as the concrete specimen is subjected to dynamic impact compressive stress wave and its multiple reflected waves. In the meantime, it is well accepted that shear strength is much greater than the tensile strength. Due to this, the original tension failure will rapidly transform to shear failure. In summary, this proves that secondary cracks are caused by tensile failure while wing cracks are caused by shear failure.

References

1. Li Yinping, Chen Longzhu ang Wang yuanhan “Experimental research on pre-cracked marble under compression.” International Journal of Solid and Structure, vol. 42, 2005, pp. 2505-2516.
2. Yin P., Wong R.H.C. and Chau K.T. “Coalescence of two parallel pre-existing surface cracks in granite.” International Journal of Rock Mechanics & Mining Science, vol. 68, 2014, pp. 66-84.
3. Casacci Susanna, Tommaso Angelo Di and Gentilini Cristina “Experimental investigation on pre-cracked masonry specimens repaired by bed joints structural repointing.” Brick and Block Masonry, 2016, pp. 2047-2054.
4. Haeri H. (2015) “Simulating the Crack Propagation Mechanism of Pre-Cracked Concrete Specimens Under Shear Loading Conditions.” Structure of Materials, 47, 618-632.

5. Pan Pengzhi, Ding Wuxiu, Feng Xiating, Yao huayan and Zhou hui "Research on Influence of Pre-Existing Crack Geometrical and Material Properties on Crack Propagation in Rocks." Chinses Journal of Rock Mechanics & Engineering, vol. 27(9), 2008, pp. 1882-1889.
6. Cao Ping, Liu Taoying, Pu Chengzhi and Lin Hang "Crack propagation and coalescence of brittle rock-like specimens with pre-existing cracks in compression." Engineering Geology, vol. 187, 2015, pp. 113-121.
7. Liu Guang, Peng Jun, Zhang Zhenhua, Wang Zhiliang and Yang Yi "Numerical investigation of fluid-driven crack propagation and coalescence in granite specimen with two pre-existing flaws." Journal of Natural Gas Science and Engineering, vol. 75, 2020, 103132.
8. W B Zhang, S Y Wang. "Dynamic numerical simulation of pre-cracked concrete samples under different mechanical parameters", Journal of Physics: Conference Series, 2021.
9. Lu C.H., Yuan S.Q., Cheng P. and Liu R.G. "Mechanical properties of corroded steel bars in pre-cracked concrete suffering from chloride attack." Construction and Building Materials, vol. 123, 2016, pp. 649-660.
10. Tirassa M., Ruiz M.F. and Muttoni A. "Influence of cracking and rough surface properties on the transfer of forces in cracked concrete." Engineering Structures, vol. 225, 2020.
11. Qu Yangdong, Li Xin, Kong Xiangqing, Zhang Wenjiao and Wang Xuezhi "Numerical simulation on dynamic behavior of reinforced concrete beam with initial cracks subjected to air blast loading." Engineering Structures, vol. 128, 2016, pp. 96-110.
12. Zhu W.C., Tang C.A. and Wang S.Y. "Numerical study on the influence of mesomechanical properties on macroscopic fracture of concrete." Structure Engineering and Mechanics, vol. 19(5), 2005, pp. 519-533.
13. Yijiang Peng, Semaoui Zakaria, Yucheng Sun, Ying Chen, Lijuan Zhang. "Analysis of Tensile Strength and Failure Mechanism Based on Parallel Homogenization Model for Recycled Concrete", Materials, 2021.
14. Haeri H. "Experimental and numerical study on crack propagation in pre-cracked beam specimens under three-point bending." J. Cent. South Univ., vol. 23, 2016, pp. 430-439.
15. Benaoum F., Kheli F. and Benhamena A. "Numerical analysis of reinforced concrete beams pre-cracked reinforced by composite materials." Frattura ed Integrità Strutturale, vol. 54, 2020, pp. 282-296.
16. Hsu Thomas T. C. "Softened Truss Model Theory for Shear and Torsion." Structural Journal, vol. 85(6), 1988, pp. 624-635.
17. Bazant Z. P. and Ozbolt J. "Nonlocal microplane model for fracture, damage, and size effect in structures." J. of Engg. Mech., vol. 116(11), 1990, pp. 2485-2504.
18. Ozbolt J. and Bazant Z. P. "Numerical smeared fracture analysis: nonlocal microcrack interaction approach." Int. J. of Numer. Met. Engg, vol. 39(4), 1996, pp. 635-661.
19. Tang, C.A. "Numerical simulation of rock failure and associated seismicity." International Journal Rock Mechanics and Mining Science, vol. 34, 1997, pp. 249–262.
20. Weibull, W. "A statistical distribution function of wide applicability." Journal Application Mechanics, vol. 18, 1951, pp. 293–297.
21. S.Y. Wang, S.W. Sloan, A.J. Abbo, M.J. Masia, C.A. Tang. "Numerical simulation of the failure process of unreinforced masonry walls due to concentrated static and dynamic loading", International Journal of Solids and Structures, 2012.
22. Wang, Shu Hong, Chun An Tang, Juan Xia Zhang, and Wan Cheng Zhu. "Implementation of a Mesoscopic Mechanical Model for the Shear Fracture Process Analysis of Masonry", Key Engineering Materials, 2005.
23. Liu, H.Y. "Numerical studies on the failure process and associated microseismicity in rock under triaxial compression", Tectonophysics, 20040616.
24. Tang, Chun'an, and Yuefeng Yang. "Finite Element Method modeling of rock dynamic failure", Advances in Rock Dynamics and Applications, 2011.
25. Mazars J. and Pijaudier-Cabot G. "Continuum damage theory — application to concrete." Journal of Engineering Mechanics, ASCE, vol. 115(2), 1987, pp. 345-365.
26. Yu-Jun Zuo, Peng Jia, Wan-Cheng Zhu, Tao Xu. "Numerical Investigation on Zonal Disintegration Mechanism around Deep Underground Openings", Advances in Mechanical Engineering, 2013.
27. Lianchong Li, Shaohua Li, Chun'an Tang. "Fracture spacing behavior in layered rocks subjected to different driving forces: a numerical study based on fracture infilling process", Frontiers of Earth Science, 2014.
28. Zhi-guang Liu, Jian-yun Chen, Wei-feng Bai, Qiang Xu. "Improved parameter selection method for mesoscopic numerical simulation test of direct tensile failure of rock and concrete", Journal of Central South University of Technology, 2010
29. W. C. Zhu, J. G. Teng, C. A. Tang. "Numerical simulation of strength envelope and fracture patterns of concrete under biaxial loading", Magazine of Concrete Research, 2002.
30. L.C. Li, C.A. Tang, W.C. Zhu, Z.Z. Liang. "Numerical analysis of slope stability based on the gravity increase method", Computers and Geotechnics, 2009.
31. Zhu, W.C and Tang, C.A. "Numerical simulation on shear fracture process of concrete using mesoscopic mechanical model." Construction and Building Material, vol. 16(8), 2002, pp. 453-463.
32. W.C. Zhu, C.A. Tang. "Numerical simulation on shear fracture process of concrete using mesoscopic mechanical model", Construction and Building Materials, 2002.

33. Zhonghu Wu, Motian Tang, Yujun Zuo, Yili Lou, Wentao Wang, Hao Liu, Wenjibin Sun. "Acoustic emission-based numerical simulation of tectonic stress field for tectoclase prediction in shale reservoirs of the northern Guizhou area, China", Energy Geoscience, 2021.
34. Zhichao Li, Lianchong Li, Bo Huang, Liaoyuan Zhang, Ming Li, Jiaqiang Zuo, Aishan Li, Qinglei Yu. "Numerical investigation on the propagation behavior of hydraulic fractures in shale reservoir based on the DIP technique", Journal of Petroleum Science and Engineering, 2017.
35. Wang, Shu Hong, Chun An Tang, Yong Bin Zhang, and Lian Chong Li. "Numerical Study on Cracking Process of Masonry Structure", Advanced Materials Research, 2005.
36. Zhao, J. "Application of Mohr-Coulomb and Hoek–Brown strength criteria to the dynamic strength of brittle rock." International Journal Rock Mechanics and Mining Science, vol. 37, 2000.
37. An, H.M., H.Y. Liu, Haoyu Han, Xin Zheng, and X.G. Wang. "Hybrid finite-discrete element modelling of dynamic fracture and resultant fragment casting and muckpiling by rock blast", Computers and Geotechnics, 2017.
38. Wang S.Y., Sloan S.W., Abbo A.J., Masia M.J. and Tang C.A. "Numerical simulation of the failure process of unreinforced masonry walls due to concentrated static and dynamic loading." International Journal of Solid and Structure, vol. 49, 2012, pp. 377-394.
39. Zhu, W.C. and Tang, C.A. "Numerical simulation of Brazilian disk rock failure under static and dynamic loading." International Journal Rock Mechanics and Mining Science, vol. 43, 2006, pp. 236–252.
40. Carpinteri, A., Lacidogna, G. and Pugno, N. "A fractal approach for damage detection in concrete and masonry structures by the acoustic emission technique." Acoustic Technology, vol. 38, 2004, pp. 31-37.
41. Tang, C.A. and Kaiser, P.K. "Numerical simulation of cumulative damage and seismic energy release during brittle rock failure-Part I: Fundaments." International Journal of Rock Mechanics and Mining Science, vol. 35(2), 1998, pp. 113-121.
42. Tang, C.A., Tham, L.G., Wang, S.H., Liu, H. and Li, W.H. "A numerical study of the influence of heterogeneity on the strength characterization of rock under uniaxial tension." Mechanical Materials, vol. 39, 2007, pp. 326-339.
43. Liu Jin, Zhongmou Wang, Renbo Zhang, Xiuli Du. "Mesoscopic simulation on flexural behavior of single-way reinforced concrete slab with rebars subjected to localized corrosion", Structures, 2021
44. Zhu W.C. "Mesoscopic numerical model for the fracture process of concrete and its application." PhD thesis, Northeastern University, China, 2001.
45. Ping Cao, Taoying Liu, Chengzhi Pu, Hang Lin. "Crack propagation and coalescence of brittle rock-like specimens with pre-existing cracks in compression", Engineering Geology, 2015.
46. Yang, S.Q.. "Experimental study on mechanical behavior of brittle marble samples containing different flaws under uniaxial compression", Engineering Fracture Mechanics, 200908.
47. Yunteng Wang, Xiaoping Zhou, Xiao Xu. "Numerical simulation of propagation and coalescence of flaws in rock materials under compressive loads using the extended non-ordinary state-based peridynamics", Engineering Fracture Mechanics, 2016.
48. Park, C.H.. "Crack initiation, propagation and coalescence from frictional flaws in uniaxial compression", Engineering Fracture Mechanics, 201009.
49. M. Cai. "Fracture Initiation and Propagation in a Brazilian Disc with a Plane Interface: a Numerical Study", Rock Mechanics and Rock Engineering, 2012.
50. Xiao-Ping Zhou, Jian-Zhi Zhang, Louis Ngai Yuen Wong. "Experimental Study on the Growth, Coalescence and Wrapping Behaviors of 3D Cross-Embedded Flaws Under Uniaxial Compression", Rock Mechanics and Rock Engineering, 2018.
51. Ha, Youn Doh, Jooeun Lee, and Jung-Wuk Hong. "Fracturing patterns of rock-like materials in compression captured with peridynamics", Engineering Fracture Mechanics, 2015.
52. S.Y. Wang, S.W. Sloan, D.C. Sheng, S.Q. Yang, C.A. Tang. "Numerical study of failure behaviour of pre- cracked rock specimens under conventional triaxial compression", International Journal of Solids and Structures, 2014.
53. P. Yin, R.H.C. Wong, K.T. Chau. "Coalescence of two parallel pre-existing surface cracks in granite", International Journal of Rock Mechanics and Mining Sciences, 2014.
54. Chuman Tang. "Numerical simulation of progressive rock failure and associated seismicity", International Journal of Rock Mechanics and Mining Sciences, 1997.
55. Zhou, X, and J Bi. "The 3D numerical study on growth and coalescence of pre-existing flaws in rock-like materials subjected to compressive loads", Transit Development in Rock Mechanics, 2014.
56. Zhou, Xiao-Ping, and Yun-Teng Wang. "Numerical simulation of crack propagation and coalescence in pre-cracked rock-like Brazilian disks using the non-ordinary state-based peridynamics", International Journal of Rock Mechanics and Mining Sciences, 2016.